Analysis of the diffuse near-IR emission from 2MASS deep integration data: foregrounds vs the cosmic infrared background

S. Odenwald[1], A. Kashlinsky[*,2], J. C. Mather[3], M. F. Skrutskie[4], R. M. Cutri[5]

[*] To whom correspondence should be addressed

[1]Raytheon ITSS, Code 685,

NASA Goddard Space Flight Center, Greenbelt, MD 20771

[2]Science Systems and Applications, Inc.,

NASA Goddard Space Flight Center, Greenbelt, MD 20771

[3]Code 685, NASA Goddard Space Flight Center, Greenbelt, MD 20771

[4]Dept of Astronomy, University of Virginia, Charlottesville, VA 22903

[5]Infrared Processing and Analysis Center, Pasadena, California

Received _____; accepted _____

ABSTRACT

This is one of two papers in which we report the detection of structure in the cosmic infrared background (CIB) between 1.25 - 2.2 μm through the use of data from the Two Micron Sky Survey (2MASS). This paper concentrates on data assembly, analysis and the estimate of the various foreground contributions; the companion paper (Kashlinsky, Odenwald, Mather, Skrutskie, Cutri 2002, hereafter KOMSC) presents the cosmological results for the CIB fluctuations and their implications. By using repeated observations of a specific calibration star field, we were able to achieve integration times in excess of 3900 seconds compared to the 7.8 seconds in the standard 2MASS data product. This yielded a point source detection limit (3σ) of $+18.5^m$ in K_s band. The resulting co-added images were processed to remove point sources to a limiting surface brightness of $+20^m$/arcsec^2 or 40 nWm^{-2}sr^{-1} . The remaining maps contained over 90% of the pixels and were Fourier transformed to study the spatial structure of the diffuse background light. After removing resolved sources and other artifacts, we find that the power spectrum of the final images has a power-law distribution consistent with clustering by distant galaxies. We estimate here the contributions to this signal from Galactic foregrounds, atmospheric OH-glow, zodiacal light and instrument noise, all of which are small and of different slopes. Hence, this supports the KOMSC identification of the signal as coming from the CIB fluctuations produced by distant clustered galaxies.

Subject headings: Cosmology: observations - cosmology: diffuse radiation - cosmology: large-scale structure of Universe - galaxies: evolution

1. Introduction

The cosmic infrared background (CIB) arises from the accumulated emissions from galaxy populations spanning a large range of redshifts. The earliest epoch for the production of this background occurred when star formation first began, and contributions to the CIB have continued until the present epoch. Apart from the cosmic microwave background, the most common source of luminosity in the universe arises in galaxies whose present-day clustering properties are fairly well known on scales up to $100h^{-1}$Mpc. The CIB, being produced by clustered matter, must have fluctuations that show the clustered nature of the underlying sources of luminosity. This signature will have an angular correlation function (or angular power spectrum) that distinguishes it from other local sources of background emission such as Zodiacal light emission, and foreground stars in the Milky Way. Moreover, distant contributions of CIB will have a different redshift, and therefore spectral color, than nearby galaxies and sources of local emission. From galaxy evolution and cluster evolution models it is possible to test the predicted slopes for the power spectrum of the CIB against the power spectrum of the data and thereby improve our theoretical understanding of galaxy evolution and cluster evolution during the first few billion years of cosmic history.

The CIB is expected to be extremely faint at wavelengths shorter than 10 μm especially when seen against the far-brighter foregrounds contributed by local matter within the solar system, as well as dust and stars within the Galaxy. A number of investigations have attempted to extract the mean intensity of the CIB from ground- and satellite-based data (see Hauser & Dwek 2001 for review). This has in nearly all instances been a complicated task due to a lack of detailed knowledge of the absolute brightness levels and their spatial variations across the sky, of the many foregrounds, and other non-cosmological backgrounds that overlay the CIB signal.

We used 2MASS calibration data to obtain long integration times and detected the

structure of the CIB in the near-IR. Much of our motivation for the current work stems from the recent surprising, and mutually consistent, discoveries of the high levels of the near-IR CIB from the COBE/DIRBE (Dwek & Arendt 1998, Gorjian et al. 2000, Wright and Reese 2000, Cambresy et al. 2001) and Japan's IRTS datasets (Matsumoto et al. 2000). Using the fluctuations method for the final COBE/DIRBE maps, Kashlinsky & Odenwald (2000, hereafter KO) measured the CIB fluctuations between 1 and 5 μm at the DIRBE beam scale ($\sim 0.7^\circ$) that significantly exceed predictions from theoretical models of galaxies with only passively evolving stellar populations.

Our presentation is divided into two parts: this paper presents a detailed discussion of the data and its assembly and the various foreground contributions and modeling. The companion paper (Kashlinsky, Odenwald, Mather, Skrutskie & Cutri 2002, hereafter KOMSC) presents the cosmological results and briefly touches on their implications.

The structure of this paper is as follows: in Section 2 we describe the 2MASS observations including their calibration, photometry and the resulting sensitivity limits obtainable from our deep integrations. In Section 3, we discuss the data analysis process, point source removal algorithms, beam deconvolution and image de-striping. In Section 4, we evaluate the sources of image noise, artifacts, atmospheric and instrumental effects. Section 5 is a discussion of the Zodiacal, Galactic and local universe backgrounds and their impact upon the detected background structure in the deep-integration study.

2. Observations

2.1. 2MASS survey

2MASS used two 1.3-m Cassegrain telescopes, one at Mt. Hopkins in the Northern Hemisphere, and one at CTIO in the Southern Hemisphere. Each telescope was equipped

with a three-channel camera, capable of observing the sky simultaneously at J (1.25 μm), H (1.65 μm), and K_s (2.17 μm) at a scale of $2''$ per pixel. As the telescopes were scanned in declination, individual 1.3-second sky frames were imaged on an overlapping grid by stepping 1/6 of the array. The frames were combined by the 2MASS data pipeline software at the Infrared Processing and Analysis Center (IPAC) to form Atlas images of size 512 × 1024 pixels with re-sampled $1''$ pixels, and an effective integration time of 7.8 seconds per pixel. Hereafter, we will use the term 'image' to refer to the calibrated 2MASS Atlas images which have been co-added to an effective integration time of 7.8 seconds.

A limited number of standard stars had to be observed repeatedly each night, and for several months at a time, to establish the photometric zero-points for the data. The 2MASS standard star fields were centered on stars from near infrared standard star catalogs (e.g. Persson et al. 1998, Casali and Hawarden 1992). Each calibration observation consisted of six independent scans of a calibration field. Each scan is a mosaic of 48 overlapping frames creating a field approximately $8.6' \times 1^\circ$ with 7.8-second integration times. The scans were made in alternating north-south directions, each displaced 5 $''$ in RA from the previous one to minimize systematic pixel effects. Repeated observations of calibration fields during a night at a variety of elevation angles were also used to develop long-term atmospheric extinction statistics.

We selected data collected at the 2MASS CTIO facility between April and August 1998 for the photometric calibration field containing the standard star P565-C. The data consisted of 2080 calibrated, overlapping images covering an $\sim 8.6' \times 1^\circ$ swath oriented north-south. The standard star region is located in the direction of RA(2000) = 16^h26^m and Dec(2000) = $+6^\circ\ 13'$. The Ecliptic and Galactic coordinates of this region are (243.5° , 27.5°) and (20.8° , 35.0°) respectively. This field is located in the constellation Hercules, 5 degrees north of the bright star λ Ophiuchus.

2.2. Photometry

A detailed description of the calibration process can be found in the 2MASS Explanatory Supplement (Cutri et al. 2001), and we now summarize the details relevant to the study of the P565-C region. The individual calibrated images were obtained from IPAC. Each image was processed in the same way as for the 2MASS Atlas Images using the same pipeline software and algorithms. To prepare the 2MASS images, each 1.3-second NICMOS camera frame had been dark-subtracted, flat-fielded and sky-illumination corrected. The calibration scans, consisting of 48 images obtained in a 1° strip in declination, were subjected to a rigorous quality control on a pass/fail basis. If a scan failed any stage of the pipeline processing, was a part of a block of observations that did not pass any of the photometric quality criteria, or if there was any evidence for clouds in the sky, the calibration scans were rejected.

Prior to co-adding each 1.3-second frame to obtain the final 7.8-second calibration image, camera pixels with poor responsivities, excessive noise, or affected by cosmic rays were masked off. For each "Read 1" (R1) and "Read 2-Read 1" (R2-R1) data frame in a scan, the appropriate nightly dark frame is subtracted, and the corresponding average "canonical" responsivity image is divided into it. Within each scan, a series of additive sky illumination corrections are derived by creating -trimmed averages for blocks of at least 42 dark-subtracted, flat-fielded sky frames. The trimmed averaging rejects any sources within the frames and yields a measurement of residual dark-sky illumination patterns on the detectors within each block. This so-called "sky offset" frame is then subtracted from each input frame, resulting in a data frame ready for source detection and combination into the final survey Atlas Images. The background levels of the final instrumentally calibrated frames correspond to the original sky levels. Before adding a frame to the output image, the image background was adjusted to match that of those images already combined into

the image by removing the median of the differences at each point in the sky in the overlap region between the current frame and the stack of already summed frames. The only background compensation made during the image construction was to adjust the frame backgrounds by a constant to produce seamless co-add images. Although the NICMOS arrays have 2″ pixels at the focal plane of the telescope, individual frames were interpolated to a 1″ grid and the resulting pixel fluxes were summed and averaged. The photometric stability of 2MASS has been determined to be $\pm 0.02^m$ (Nikolaev et al. 2000). The majority of the images for our survey field were obtained at air-masses between 1.2-1.7 and elevation angles of 40-60° .

We converted from magnitudes given in the 2MASS J, H and K_s bands to brightness units in terms of nWm^{-2}sr^{-1} by using the zero-magnitude J, H and K_s-band factors from Cohen (2001, private communication) of F_0 = 1592, 1024 and 667 Jy with an uncertainty of ±1%. We also note that, based on the preliminary absolute calibration constants for the 2MASS, J, H and K_s bands, the conversion to AB magnitudes becomes, $m(AB) = m_J + 0.90, m_H + 1.37$ and $m_{K_s} + 1.84$ respectively.

Variations in the sky background conditions spanning the five months of data obtained for the P565-C field can be identified from a histogram of the background pixels in each calibrated field. The shape of this peak was fit by a simple Gaussian to determine the mean background level for the frame, and the dispersion of the background emission. This mean level was then subtracted from each pixel to obtain an image with a zero mean background intensity so that it could be co-added with the other frames from this sky region. The mean level-subtracted frames were co-added onto a grid with 1″ pixels using the individual frame center coordinates as a guide to registering the images. In Figure 1 we show the histogram of the fitted dispersion for each of the images used in this analysis. The data quality as measured by the dispersion of the Gaussian background fit for each of the 2080 calibrated images shows that for J and K_s bands, the typical dispersion is ≈ 30-70 nWm^{-2}sr^{-1} for

more than 90% of the frames. The H-band data, located near the peak of the OH air-glow atmospheric emission, was predictably noisier than either the J or K_s data with a much broader dispersion of 100-150 $nWm^{-2}sr^{-1}$. Although the mean intensity of the OH-glow is significant, we found that during the course of the co-addition process, the noise in this component integrates down with N images co-added as $N^{-1/2}$.

The 2080 calibrated images were co-added into a final 'deep-integration' image by using the coordinate information for the center of each image, and performing a pixel-by-pixel summation of the intensities. Each image was corrected for its own calibrated zero point provided in the image header field to place the photometry on a common scale. We also counted the number of measurements that were used in a given pixel to establish a statistical weighting function for the summed and averaged data which was used in subsequent stages of the analysis. Figure 2 gives the histogram of the number of images available for each pixel, while Figure 3 shows the final averaged map. The typical number of samples per pixel is ≈ 500 for an equivalent integration time of ≈ 3900 seconds. The top three images show the J, H and Ks data for a single 7.8-second calibration frame. The lower three images are the corresponding deep-integration fields.

The final co-added field was $536'' \times 3567''$ in size with $1''$ pixels. For purposes of Fourier analysis and the computation of the angular power spectrum, the field was cropped into seven 512×512 pixel patches. This cropping also removed most of the edge-effects caused by the mosaicking and co-adding process. For example, because each calibration scan is offset 5 $''$ in Right Ascension from the previous scan, pixels within 30 $''$ of the east and west edges of the final image are observed significantly less often than pixels within the bulk of the image. The patches are numbered 1–7 and are shown in Figure 4.

Photometry of a random selection of 180 stars in Patch 3 (shown in Figure 3) of the field yields the [J-H]: [H-K_s] color-color diagram indicated by the diamond symbol in Figure

5(a). The brighter stars in this field had $K_s = +11.0^m$ (S/N $\approx$ 286). Near the 2MASS point source limit of $K_s = +14.5^m$, stars were detected at a typical S/N of $\approx$ 70. Also shown in the figure are the colors for a sample of objects in the 2MASS Point Source Catalog at a Galactic latitude of $b^{II} = 78^\circ$ with $K_s > +14^m$, and $S/N > 10$. The elliptical ring indicates the extent of the distribution for $\approx 10^5$ stars. The majority of the stars in Patch 3 were detected at low S/N. The photometered stars in Patch 3 appear to have colors similar to the ones in the larger 2MASS survey. This finding is also borne out in Figure 5(b) which shows the [H-K_s] color compared to K_s for the faintest point sources within our sample.

2.3. Sensitivity Limits

According to the 2MASS Explanatory Supplement, a typical 7.8-second Atlas image achieves a 10-sigma detection limit of J = 15.8^m (0.7 mJy), H = 15.1^m (0.9 mJy), and K_s = 14.5^m (1.2 mJy). The photometry of the faintest stars in our deep-integration fields shown in Table 1, along with their S/N values in parenthesis, allows us to deduce limits nearly 4.0^m fainter in each band than the standard 2MASS sky survey images.

By extrapolation from the 2MASS survey photometry, in K_s band, at a detection limit of 10σ, the 2MASS point source magnitude limits for the final images will be $+17.7^m$ for a background noise that integrates down as $t^{-1/2}$. In J and H band, these limits are $+19.2^m$ and $+18.5^m$ respectively. Generally, the deep-field point source detection limits are consistent with those expected from the original 7.8-second Atlas Images when allowance is made for the increased integration times alone. The equivalent AB magnitude limit corresponding to the actual 10σ J, H and Ks band deep-integration limits of $+19.6^m, +19.7^m$ and $+17.7^m$ are $m(AB) = +20.5^m, 21.1^m$ and $+19.5^m$ respectively.

2.4. Point Source Removal

With 2MASS and its arc-second-scale resolution, the images of bright stars and nearby galaxies can be readily separated from their neighbors and removed. The seven patches in our 2MASS fields were de-sourced independently using the following algorithm:

We computed the dispersion σ of the pixel intensities for each of the seven patches. Then pixels with flux exceeding a fixed number of standard deviations ($N_{\rm cut}$) were removed, along with their 8 nearest neighbors. The process was repeated for all pixels within the image, then the dispersion was recalculated to produce the σ for the next iteration. This iterative algorithm was repeated until no further pixels were found. Typically, only 3-5 iterations were needed for the process to converge to a final de-sourced map. We experimented with $N_{\rm cut} = 3, 4, 5$ and they all gave practically identical results. The results below will be presented for $N_{\rm cut} = 3$.

The magnitude limits of our iterative clipping process can be obtained for a given σ in $\mathrm{nWm^{-2}sr^{-1}}$ by converting the pixel surface brightness limit into an equivalent magnitude per square arc-second for a perfectly unresolved star located at the center of the pixel. For $\sigma = 50$ $\mathrm{nWm^{-2}sr^{-1}}$ in J-band, this corresponds to an integrated brightness of a $+23.8^m$ star within a one square arc-second solid angle. Similar calculations yield $+23.0^m$ and $+22.2^m$ in H and K_s bands. The corresponding $m(AB) = +24.7^m, +24.4^m$ and $+24.0^m$ respectively. The measured peak surface brightness of an unresolved source seen by 2MASS typically accounts for 10 % of the detected emission. This means that actual point source magnitude limits for the clipping process are 2.5^m brighter than the magnitude limit calculated from the peak surface brightness and the clipping parameter.

Table 2 shows the result of applying the clipping procedure to P565-C in the K_s band and for all seven patches. Column 1 identifies the patch number oriented from south (1) to north(7) along the calibration field. Column 2 gives the percentage of pixels that survived

the clipping operation. Column 3 gives the average number of 7.8-second observations per pixel. In the next three columns we indicate the surface brightnesses that correspond to the clipping level at σ which is given in nWm^{-2}sr^{-1} in parenthesis. (e.g. 36 nWm^{-2}sr^{-1} corresponds to a K_s surface brightness of $+20.1^m$/asec^2 and a point source magnitude of $+19.7^m$). For a clipping threshold of 3σ, all point sources 1.2^m brighter than the magnitudes shown in Table 3 were removed. Typically, more than 90% of the pixels in each patch survived the point source clipping process with 3×3 pixel masking. Given the 7.8-second integration per sample, we see in column 3 that the typical integration times for the patches were in the range from 3,682 - 4,056 seconds.

Figure 4 shows the resultant images in the three 2MASS bands. The seven clipped patches ordered from bottom to top are shown in the left-side panels in each band. The masked pixels eliminated by the clipping algorithm are shown in black. The right-side panels in each band show the maps of the number of co-adds that went into each pixel.

3. Analysis

If the CIB is generated by clustered, luminous matter in the distant universe, the structure of the CIB should contribute to the angular correlation function of the background noise fluctuations of the diffuse light in the J, H and K_s band data following the removal of the point sources. An alternative, and faster, method of characterizing the angular intensity distribution is to determine the power spectrum of the 2MASS data, which is the Fourier transform of the angular correlation function.

The fluctuation in the CIB surface brightness can be defined as $\delta F(\boldsymbol{x}) = F(\boldsymbol{x}) - \langle F \rangle$, where $F = \lambda I_\lambda$, $\boldsymbol{x}$ is the two dimensional coordinate on the sky and $\langle F \rangle$ is the ensemble average. The two-dimensional Fourier transform is $\delta F(\boldsymbol{\theta}) = (2\pi)^{-2} \int \delta F_q \exp(-i\boldsymbol{q} \cdot \boldsymbol{\theta}) d^2\boldsymbol{q}$. If the fluctuation field, $\delta F(\boldsymbol{x})$ is a random variable, then it can be described by the

moments of its probability distribution function. The first non-trivial moment is the projected 2-dimensional correlation function $C(\theta) = \langle \delta F(\boldsymbol{x} + \theta) \delta F(\boldsymbol{x}) \rangle$. The 2-dimensional power spectrum is $P_2(q) \equiv \langle |\delta F_q|^2 \rangle$, where the average is performed over all phases. The correlation function and the power spectrum are a pair of 2-dimensional Fourier transforms and for an isotropically distributed signal are related by

$$C(\theta) = \frac{1}{2\pi} \int_0^\infty P(q) J_0(q\theta) q dq, \tag{1}$$

$$P(q) = 2\pi \int_0^\infty C(\theta) J_0(q\theta) \theta d\theta, \tag{2}$$

where $J_n(x)$ is the n-th order cylindrical Bessel function. If the phases are random, then the distribution of the brightness is Gaussian and the correlation function (or its Fourier transform the power spectrum) uniquely describes its statistics. In measurements with a finite beam, the intrinsic power spectrum is multiplied by the window function W of the instrument. Conversely, for the known beam window function, the power spectrum can be de-convolved by dividing the measured power spectrum by the beam window function.

After Fourier transforming the clipped maps, we computed the power spectrum for each of the seven patches by averaging the square of the Fourier amplitude in concentric rings around a given wavenumber q. The amplitudes were weighted by the number of measurements available for each pixel in the co-added, 2MASS field. In Figure 6 we show the power spectrum of the data for Patch 3 with point sources clipped at 3σ, and for an equivalent integration of 7.8 seconds. The expected small-angular scale behavior is dominated by the beam point-spread function. The large angular scale power spectrum is essentially flat, consistent with white-noise distributed fluctuations. At this very short exposure, the sensitivity of 2MASS is not sufficient to register large-scale zodiacal or cosmological structure, and only the apparently random and uncorrelated structure of the instrument+atmosphere background emission are expected to contribute. The sensitivity in a single 7.8-second image is, however, adequate to detect stars and galaxies at small

angular scales, where we see a power spectrum that resembles white noise multiplied by the instrument beam profile. The beam window function can thus be determined very accurately and the power spectrum de-convolved. The de-convolved power spectrum is shown with plus signs.

Figure 7 shows the de-convolved power spectrum of the deep-integration clipped Patch 3 in K_s band with Poissonian error bars (i.e. $\delta P/P =$[number of points within dq of q]$^{-1/2}$). The "x" signs correspond to the maximal exposure clipped images. The filled diamonds correspond to the atmospheric contribution to the power spectrum (i.e. the power spectrum from one co-add divided by the mean number of co-adds for this patch). One can clearly see the excess power, and the different slope of the power spectrum, for the diffuse emission in the co-added image. This suggests a significant contribution from background infrared emission below the clipping threshold which includes the CIB emission. Similar results obtain for the 2MASS J and H bands.

As Figures 3 and 4 show, there are residual stripes in the long-exposure images. Such stripes arise from variety of known instrumental effects including diffraction within the telescope optics, and electronic crosstalk in the presence of bright stars. In Fourier space, the horizontal and vertical stripes collapse onto the wavenumber axis, corresponding to zero frequency in either horizontal or vertical direction. Figure 8 shows the Fourier map of the maximal exposure Patch 3 in K_s band. Similar maps obtain for J and H bands and are not shown for brevity. The Fourier transform of the stripes is clearly seen in the cross-pattern along the axes. In order to de-stripe the images and compute the underlying power spectrum for the diffuse emission, we excised the narrow strip of pixels along each axis of the Fourier transform. The final power spectra are not sensitive to the width of the removed strip, and in what follows we present the numbers with 2 pixels removed in the Fourier plane along each axis.

Figure 9 presents the variation of the background fluctuation dispersion in each of the seven clipped patches before and after de-striping for the J (triangles), H (squares) and K_s (crosses) bands. The de-striped and "raw" dispersions are proportional, which means that the removed variance due to stripes does not come from the residual sky emission.

Figure 10 shows the final power spectrum of the diffuse emission in the seven patches of the field after de-striping. The expected atmospheric power spectrum for the final co-add would be given by the power spectrum at 7.8 sec (Figure 6) divided by the number of co-adds in the final maps and shown with filled diamonds. The final rms fluctuation in the surface brightness for the patch after de-striping is is shown in the upper left corner of each patch in units of nWm^{-2}sr^{-1} . The persistence of a distinct power law and its similarity in each band shows that it is a robust signal reflecting a common background structure in this direction of the sky.

Note that our method subtracts out the mean (DC) level of the background, including the CIB. The latter therefore cannot be constrained directly by the fluctuations method. However, the DC levels of the near-IR CIB have been measured directly from the COBE/DIRBE and IRTS data. E.g. they give ca. 50 nWm^{-2}sr^{-1} in J band (Cambresy et al 2001), ca. 25 nWm^{-2}sr^{-1} in K (Wright & Reese 2000) and are consistent with the IRTS measurements of the CIB mean levels between these bands (Matsumoto et al 2002). We clip galaxies out to K$\sim 18.5^m - 19^m$ so the clipped galaxies contribute only $\lesssim$6 nWm^{-2}sr^{-1} and the K-band galaxies observed down to the faintest magnitude of $K \sim 24^m$ contribute $\sim$ 9 nWm^{-2}sr^{-1} (see Fig. 2 of KOMSC). In principle, the mean level of the CIB can be constrained from the TEV gamma-ray measurements of galaxies with known energy spectrum (Stecker & De Jager 1993), but these constrain the CIB mean levels most effectively longwards of 5 μm, where no direct measurements of the CIB mean levels currently exist.

4. Non-Cosmological Contributions

It is clear from Figure 6 that the final images contain a diffuse infrared component with a power spectrum that is distinct from the white noise contributed by the atmosphere+instrument background and by stars. We now investigate some of the potential sources of this signal, and assess their contributions.

4.1. Atmospheric Effects

The largest contribution to the sky background comes from the atmosphere itself, which for a single 7.8-second integration at K_s band amounts to 295 MJy/sr or equivalently $+12.4^m$/arcsec^2. The spectrum of the emission has the color shown in Figure 4 represented by the square plotting symbol and is dominated by a combination of atmospheric and instrumental thermal emission. The 2MASS frames preserve the observed background sky levels measured relative to camera dark frames with the shutter closed. This background is normally largest in the K_s band, although it can be even larger in the H-band due to atmospheric OH air-glow emission. The only background compensation made during Atlas Image construction is to adjust the six survey frame backgrounds by a constant to produce seamless co-added Atlas images with 7.8-second integration times. Because the OH air-glow (especially at H-band) contains structure on scales at, or below, the 2MASS frame size, the resulting 2MASS Atlas images often show large background variations. According to Ramsay et al. (1992) the variation of OH-glow due to gravity waves occur at angular scales of about 17 degrees and with time scales of 11 minutes. 2MASS analysis of short-term, background noise characteristics in the Atlas images suggests that much finer spatial scale variations also exist.

Since variations of the mean atmospheric background level contribute to increasing the

final background noise of the co-added image, we removed this component in the individual images via a simple Gaussian fit, which determined the amplitude and dispersion (σ) of the background pixel intensities in each image. This Gaussian fit was truncated at the high end to eliminate the contributions from stars. We then subtracted the Gaussian-fitted, mean background intensity from each pixel. Thus all information about the mean intensity of the background has been removed from the final co-added data, including any information about the mean intensity of the various astronomical backgrounds. We can, however, evaluate the contributions by some of these backgrounds to the 'noise' of the final co-added image.

The image dispersions determined from the individual Gaussian fits were compared with airmass in Figure 11 to determine whether any obvious trends existed in the data that could suggest a correlated atmospheric 'signal' spanning the five months of data. No apparent correlations were identifiable. Given a mean sky background noise near ≈ 300 MJy/sr in K_s band, Figure 11 shows that over the course of 5 months, the background noise was surprisingly uniform (typically ± 500 nWm^{-2}sr^{-1}), and varied by less than ± 100 nWm^{-2}sr^{-1} . In H-band where OH-glow dominates, the variation of the background noise was ± 1000 nWm^{-2}sr^{-1} for a mean sky intensity of 140 MJy/sr .

Figure 12 shows the histogram of the residual pixel intensities, F, in Patch 3 after clipping, where we define the probability density as the ratio of the number of pixels in the $[F; F + dF]$ range of brightness to the total number of pixels in the patch. Although the individual images that make up the co-added image have been corrected to a zero mean computed in the absence of stars, the histograms show the effect of the variation of image-to-image pixel noise for the co-added sample. The histograms have offsets of 190, 250 and 330 nWm^{-2}sr^{-1} for K_s, J and H-bands respectively. This corresponds to the dispersion of the individual frame background noise values shown in Figure 11 determined in a consistent manner for the pixels in Patch 3. It is also evident that the histograms are

smooth and Gaussian-like with some evidence for tails toward larger values resulting from the remaining un-clipped point source emission. This indicates that transient atmospheric conditions leading to increases in the individual image noise are sufficiently Gaussian for our purposes, with no long-term correlation over the 5-months of data.

Figure 5(a) shows that, based on the color of the atmospheric component (box symbol with 1-σ error bars) determined from the 2080 individual images of [J-H] = $+1.9^m \pm 0.4^m$ and [H-K_s] = $+1.2^m \pm 0.4^m$ it is also evident from the colors of the residual emission in Patch 3 and plotted with an asterisk (e.g. [J-H] = $+0.07^m$ and [H - K_s] = $+0.57^m$) that no trace of an atmospheric component remains in the final data. This confirms that by removing the mean background from each image prior to co-adding, we have eliminated the majority of the atmospheric contamination. The mean residual background intensity in K_s band was 0.14 MJy/sr or equivalently 190 nWm^{-2}sr^{-1} and $+20.8^m$/asec^2, which is less than 0.05% of the original sky background detected in a single 7.8-second image. This confirms the long-term stability of the atmosphere and shows that its properties can largely be assumed to be uncorrelated in both space and time over the angular scales we are investigating in this study.

4.2. Instrumental Effects

The data that we use span over 5 months of observations. As a consequence of the observing protocol, the telescope was moved $5''$ in RA during each N-S scan, and the mosaicking process insured that, in the regions of overlap, multiple array pixels were used to measure the brightness of a particular line of sight. The more than 500 brightness measurements made in a typical pixel of the final deep-integration image are the product of measurements made by ≈ 20 different pixels in the array itself, thereby reducing greatly the possibility of systematic gain and responsivity effects entering the final image.

We can characterize the short-term instrument and background changes which lead to non-zero residual emission in the co-added images by simply differencing the 'odd' and 'even' images in the 2MASS data on a pixel-by-pixel basis. We refer to these difference maps as A–B maps. Observationally, we have for every pixel, a time-ordered string of measurements that were averaged together to obtain the pixel value in the deep-integration image. We can separate this string of measurements, one per image, into an even and an odd series, and subtract the individual pairs of measurements. In doing so, we remove any time-independent component which appears as a mean 'DC' level. The new image based on these differences is now a repository for any background component that varied over the course of consecutive nightly measurements of the same pixel. For example, if the background conditions during a single night varied significantly due to changes in OH-glow between the consecutive observations of the calibration field, a non-zero A–B residual will occur for some or all the pixels in the calibration strip. If this difference persists over the course of many nights, then the long-term average of the A–B over the full data will produce a statistically significant residual. Instrumental effects, such as long-term responsivity changes and drifts will also be included if the conditions changed during the course of consecutive nights of observation.

Figure 13 shows the resulting A–B co-added image for Patch 3 in K_s band, masked according to the clipped output to remove regions containing emission from point sources. The residual emission in the un-blanked portions correspond to ~ 2 nWm^{-2}sr^{-1} for the 2MASS bands. In Figure 14, the power spectrum of the A-B image confirms that there is essentially no correlated signal in the background data that might be contributed by instrumental variations or intra-day variations in atmospheric emission. The power spectrum is white noise modulated on small scales by the window function due to IPAC interpolation to the $1''$ pixels.

Latent star-like images can be created by the NICMOS detector material after exposure

to bright stars. The decay time constant is about 10 seconds. This process produces a string of point sources of decreasing brightness that are spaced with offsets that match the 83.3″ sequential steps used in creating the overlapping frames at the telescope. After final processing of the deep-integration images, we see no signature of this feature in the power spectrum.

Internal telescope reflections can also produce stripe/streak features extending over 1° in radius from the bright star's center. Internal reflections of bright stars or other starfield-dependent instrument artifacts cannot account for the detected fluctuation power spectrum. As we noted in Section 3.1, there is no evidence that the variation of unclipped artifacts in the seven patches (e.g. Patch 2,6,7 vs. Patch 3,4,5) leads to a significant change in the power-law feature seen persistently across all the patches and bands, at least over angular scales from 2″ to 100″ .

As a consequence of a variety of transient events such as cosmic ray hits, and meteor streaks, the 2MASS images are automatically blanked by the 2MASS pipeline software wherever such 'bad pixels' appear. This means that the number of samples per pixel in the initial Atlas images may be less than the canonical value of 6 for some small percentage of the pixels in the field. This impacts the actual effective integration times used in calculating our final co-added, background noise averages across the field. Since fewer than 1 % of the pixels are typically involved per 1.3-second exposure, and since there is no correlation of these events across the full 5-month archive of images, these pixels are randomly distributed across the image and do not contribute to a systematic 'pattern noise'. This is also apparent in the white noise-character of the co-added image power spectrum at scales of a few arcseconds where pixel blanking would normally contribute.

The difference maps over the area remaining after source clipping give flux dispersions a factor > 10 lower than that of the co-added clipped images. E.g for patch 3 we get

$\sigma = (2, 3, 2)$ nWm^{-2}sr^{-1} in J, H, K_s bands respectively. This adds in quadrature to the variance from other terms including the CIB. Thus the instrument noise is negligible compared to the signal in Figure 10.

4.3. Stray Light

We considered the possibility that stray light and stray electronic signals in the telescope and instrument could mimic large scale fluctuations. Even the ideal Fraunhofer diffraction point source response function from a telescope falls off with angle only as $1/\theta^3$, and the integral of the light outside θ falls off only as $1/\theta$. Diffraction from dust grains and other imperfections on the optical elements, and in the Earth's atmosphere, may be expected to have similarly slow asymptotic behavior. Hence an experimental test is required.

We therefore found 2MASS observations of several bright star fields near the Galactic plane where the star density after 7.8 sec exposure is comparable to our Patch 3. The fields, 1 degree in radius, were located at the J2000 coordinates (RA , Ded) = (19^h 18^m 23.6^s, -37° 5′ 30″) and (18^h 6^m 32.0^s, -39° 31′ 19.7″). The short exposure images of these regions look qualitatively much like the long exposure co-adds in darker regions, and we expect that the stray light and stray electronic signals should also resemble those in our deep regions when properly scaled. We analyzed these data with the same clipping algorithms and computed the residuals. The clipping algorithm leaves behind about the same number of pixels (94%) as for our deep exposures. However, we found that the clipped power spectra are almost perfectly flat, except for the very largest spatial scales. This clear qualitative difference shows that stray light does not explain the slopes of our measured fluctuation power spectra. The clipping algorithm leaves power spectrum residuals that are 2.4 to 3.3 orders of magnitude lower than the unclipped power spectra, showing that at least 93% of

the total flux of each star is removed by the algorithm.

Figure 15 shows these results, comparing the unclipped and clipped power spectra of our one such long exposure region (Patch 5) with the results of the bright star field from the main 2MASS survey, scaled to match the unclipped power spectra. The scaled clipped bright star field power spectrum is significantly fainter than the long exposure region, showing that stray light from the stars is unlikely to cause the measured fluctuations on large angular scales.

All the patches on close visual inspection showed residual extended halos around the brightest stars. To test whether extended halos around stars cause a significant effect on the power spectra, we analyzed Patch 3 with SExtract, determined the list of sources and their isophotal diameters, and made a new map with square masks with edges that were four times the isophotal diameters. We then computed the power spectra again. The result was within 2% for scales below 1 $''$, with a decrease of 10% at 10 $''$. While these changes are within the error bars, they do show a small trend, and would change the power spectrum slope by about 0.04.

4.4. Zodiacal Emission

At wavelengths from 1.25 to 2.2 μm the emission from interplanetary dust is dominated by scattered sunlight which declines in brightness by 3-fold over this wavelength range. DIRBE photometry in the direction of the 2MASS field obtained near a solar elongation angle of 90° yields an integrated K-band background of ~ 150 nWm^{-2}sr^{-1} with a spectrum dominated by scattered Zodiacal light (ZL). Moreover, the color of the ZL follows the solar spectrum to ≈ 2 μm . In Figure 5(a), the color of ZL is also indicated (large triangle symbol) and it is clear that the residual background seen in the 2MASS co-added image is significantly redder. This indicates that any residual sky contribution by ZL to the final

co-added image appears to have been subtracted out during the co-adding process itself. Indeed, because we are only concerned with the detection of structure in the CIB, some amount of ZL can be tolerated in our analysis provided that this emission is smooth over the angular scales of interest. In our analysis, we are not concerned with the absolute magnitude of the ZL but rather with its angular structure at 2MASS scales from $2''$ - $100''$. It is generally believed that ZL is smooth at these scales due to a variety of physical mechanisms (e.g. Poynting-Robertson drag, orbital phase diffusion) which act to smooth out dust irregularities which would appear at these scales.

Cometary dust bands are known to exist at $\beta < |10^\circ|$ with half width of $\approx 3^\circ$ (Reach, 1992). These features are significantly below the latitude of the 2MASS field and are not relevant to this study. Some claims have been made for fainter bands at $\beta = \pm 22^\circ$ (Sykes, 1988) but these have not been confirmed in other studies. In all cases, the banded features are degree-scale features, prominent in the mid-IR near 25 μm and are not known to contribute to scattered light emission in the 1-2 μm range. A resonant dust ring outside Earth's orbit was detected by DIRBE at 4.9 - 25 μm (Reach et al. 1995), however, its emission peaks at 25 μm , and at 4.9 μm its excess surface brightness above the local Zodiacal background is ≈ 0.05 MJy/sr (30 nWm^{-2}sr^{-1}). This feature is located at an elongation angle of 90° and extends 15° in longitude with a 30° FWHM in latitude. This places the 2MASS region outside the zone where the emission from this feature predominates.

Studies of the arcminute-scale angular structure of the ZL by Abraham, Leinert and Lemke (1998) with the ISO/ISOPHOT instrument also indicate that at 25 μm , no structure can be detected above 0.2% of the total ZL brightness in a number of fields distributed over a range of Ecliptic latitudes. Because the thermal emission is optically thin and the dust grains are essentially isothermal, the distribution of the scattered light should follow the variations in the thermal emission. Based on a total 2.2 μm surface brightness

for the ZL of 130 nWm^{-2}sr^{-1} from DIRBE photometry, and the limit set by the structure at 25 μm , we expect that ZL structure will not contribute more than ≈ 1 nWm^{-2}sr^{-1} in the 2MASS bands on arc-minute scales.

The 2MASS observations which were used in this study, span a time period from April to August and a solar elongation range from 115° to 128°, which means that any persistent Zodiacal structure would become uncorrelated during the data averaging process. We, therefore, conclude it is unlikely that sub-arcminute structure in the Zodiacal background emission is present in the 2MASS data in the form of a well-defined power spectrum.

4.5. Interstellar Dust

Although interstellar cirrus is primarily a feature of the far-infrared sky, the presence of PAH emission in cirrus material allows some interstellar clouds to contribute to the infrared backgrounds even at near-IR wavelengths. Studies of PAH emission show a spectral feature at 3.3 μm and no other identifiable lines at 1-2 μm in the 2MASS band-passes. This implies that there is no radiation mechanism capable of producing foreground emission within the 2MASS bands that could generate infrared background fluctuations. Moreover, investigations of the angular structure of cirrus emission have found structure as small as the IRAS resolution limit near 2 arcminutes. Gautier et al. (1992), Wright (1998) and KO find that cirrus follows a power law of the form $P(q) \propto q^{-n}$ where $n \approx 2.5 - 3.0$. In addition Guhathakurta & Cutri (1994) find that the power spectral slopes of the cirrus emission detected in the optical V band down to a few arcsec scale was the same as for the IRAS emission at long wavelengths. This shows that the cirrus structure at small scales and shorter wavelengths, probed by the 2MASS survey, is consistent with the longer-wavelength characterizations.

Interstellar dust can, in principle, cause extinction effects that under some circumstances

could modulate the light from a more distant and uniform star background, giving rise to structure in the infrared background. Because the amount of extinction varies strongly with wavelength, the strongest fluctuations caused by a clumpy interstellar medium would occur in J-band, and with declining strength in H and K_s bands. No such wavelength-dependent variation in the power spectra in Figure 10 is apparent. At K_s band, models for the amount of interstellar extinction indicate about A = 0.05^m and a differential extinction across the 1° field of $\approx 0.005^m$. This would correspond to a modulation of a uniform background source by 0.5% at the 1°-scale. Smaller-scale extinction variations with a higher amplitude may also be possible if the mechanism involved (e.g. cirrus) has structure at these scales. We can estimate the amplitude of the 1° component by assuming that, at most, the background emission is produced by unresolved stars below the clipping threshold. From Table 2, a typical clipping threshold (3σ) is about 150 nWm^{-2}sr^{-1} so that for a 0.5% modulation of the extinction one obtains an amplitude of about 1 nWm^{-2}sr^{-1} .

4.6. Diffuse Galactic Starlight

As we note from Table 2, the 3-σ clipping threshold in Patch 3 eliminated stars brighter than approximately $+18.5^m - 19^m$ in K_s-band. The color-color and color-magnitude diagrams in Figures 5(a) and 5(b) show that the properties of the extracted point sources are consistent with ordinary stars. We can compute the [J-H] and [H-K] colors of the residual noise in the clipped fields which amounts to 351 ± 55, 236 ± 48 and 196 ± 34 nWm^{-2}sr^{-1} for J, H and K_s respectively, which leads to [J-H] = $+0.07^m$ and [H-K_s] = $+0.57^m$. In Figure 5(a) we find this color to be distinct from Zodiacal light emission ([J-H] = $+0.4^m$ and [H-K_s] = -0.4^m), or atmospheric emission ([J-H] = $+1.9^m$] and [H-K_s] = $+1.2^m$), but similar to that of the population of point sources that were photometered. In fact, it is similar to the color of K0V stars ([J-K] = $+0.64^m$).

Based on the photometry of the point sources in Patch 3, we can determine the star count distribution for this region and compare it with star count models to assess how much starlight remains in the field after bright-source clipping. We have calculated the expected star counts in the direction of the 2MASS field by employing the Faint Source Model (FSM) developed by Arendt et al. (1998) for the analysis of the COBE/DIRBE data. The FSM is based on the five-component galaxy population model described by Wainscoat et al. (1992). Given the galactic coordinates of the field, only two components contribute to the star counts: A halo population and a disk population. The FSM model consists of 87 types of stars spanning a luminosity range $-6.0 \geq M_v \geq +8.5$, and assigned to each of the structural components as appropriate. An integral is performed along the line-of-sight to the specified region, and at each distance increment, a calculation of the number of stars and their apparent magnitudes is performed. The results are stored in an array that yields the cumulative number of stars brighter than magnitude m, $N(m)$ and is presented in Figure 16. We also show in the same figure the actual star counts obtained in 6 magnitude bins within Patch 3. Due to the small number of stars brighter than $+16^m$ in this $8' \times 8'$ field, the statistical error bars for the brightest two bins are significantly larger than for the fainter bins plotted. Generally, the actual star counts follow the predicted counts quite closely over the range from $+16^m$ to $+20^m$. We note, however, that the most significant counts between $+17^m$ to $+19^m$ are higher than the predicted counts, reflecting the fact that faint galaxies should enter the statistics for these fainter counts.

Because Galactic stars have a white noise spatial distribution, the flux fluctuation, σ_* from stars brighter than $m_{\rm cut}$ is given by: $\sigma_*^2 = \omega_{\rm beam}^{-1} \int_{m_{\rm cut}}^{\infty} I_\nu^2(m) n(m) dm$ where $\omega_{\rm beam}$ is the 2MASS beam area, $n(m)dm$ is the number of stars within dm of the apparent magnitude m and $I_\nu(m) = I_{\nu,0} 10^{-0.4m}$ is the intensity of a star of magnitude m at frequency band ν. Using a Galactic model normalized to 2MASS, we estimate that stars fainter than $m_{\rm cut} \geq 18.5$ would contribute less than $\sigma_* < 9 {\rm nWm^{-2}sr^{-1}}$ to the total fluctuations. This

component adds in quadrature to the total dispersion, thus contributing less than 2-3 % of the total signal in the co-added maps.

The power spectrum of an unclipped sky patch, which is dominated by the emission from foreground stars, shows that stars are not clustered, but have a white-noise spectrum for angular scales $1''$ - $100''$. Our study of the properties of the remaining point sources near, or just below the $3-\sigma$ clipping threshold indicates colors that appear to be similar to those just above this threshold, and we conclude that there is no firm evidence that the unresolved stars contributing to the diffuse emission in the field are a different population than the bright stars that were removed, or that they have different clustering properties. Although the diffuse stellar component dominates the background light, it is not structured in a way that is expected to lead to a power-law spectrum.

We checked whether the imperfect blanking of starlight in the field may have had an impact upon the resulting power spectrum. We examined this in several ways : 1) we ran the source extractor from the COBE DIRBE fluctuations work (see KO for discussion), 2) employed the widely-used package SExtractor (Bertin and Arnouts 1996) to identify discrete sources in the 2MASS fields, and 3) simulated the effect of the residual halos on the large scale power spectrum of the diffuse emission. The SExtractor algorithm produces a file which specifies the integrated magnitude, location and shape of all extracted sources brighter than a user-specified S/N. We used this information to create a mask of all the discrete sources, and this was then used to blank out the sources. SExtract identified 581 discrete sources brighter than 3-σ in Patch 3 at K_s band, which corresponded to a masking of 19,160 pixels or 7.5% of the total field area of Patch 3. This is identical to the level of masking obtained by our clipping algorithm. Figure 17(a) shows that the angular radii of the sources determined by SExtract are $<2''$ and therefore unresolvable by 2MASS. Figure 17(b) also shows the variation of the rms source radius with integrated K_s magnitude determined by SExtract, which indicates that the fainter sources in this

study are substantially unresolved. A comparison of the first two procedures showed agreement between the sources that were blanked. SExtract was more efficient in removing the extended faint halos of the brighter stars from the sky data, however, there was no practical effect on the power spectrum of the diffuse emission for the remaining field pixels. Nevertheless, we checked by independent simulations that the remaining halos do not mimic the observed signal. The halos retain the white noise distribution of the underlying Galactic stars and would produce the white power spectrum on scales outside the 2MASS beam ($\sim 2''$) contrary to what is measured in Figure 10.

4.7. Nearby Galaxies

The nominally complete 2MASS sensitivity limit at 10-σ to galaxies as point sources is $K_s = +14.5^m$ (or $+16^m$ at 3-σ). Studies by Huang et al (1997) and Cowie et al. (1996) with the Hawaii K-band Galaxy Survey and a magnitude limit of $K < +16^m$ find a corresponding redshift limit near z $\approx$ 0.2. There are no discernible bright galaxies in the P565-C field of view with near-IR diameters significantly larger than $\approx 5''$, and magnitudes brighter than $\approx +16^m$ which indicates that in this sky direction there are no large ($r \approx$20 kpc) galaxies closer than $\approx 400\ h^{-1}$Mpc ($\theta = 5''$; z $\approx$ 0.1). At the fainter magnitudes covered by this survey, the situation becomes more complicated.

Field spheroidal galaxies with $M \approx 10^{11} M_\odot$ are expected to correspond to objects with $+18<K<+20$ and a redshift range $1<z<2$ (Kauffmann and Charlot 1998, Jimenez & Kashlinsky 1999, KOMSC). The Hawaii Medium Deep Survey covers 170 arcminutes^2 to a magnitude limit of K = +19. Spectroscopic studies of the galaxies in this field by Cowie, Songaila, Hu and Cohen (1996) show an approximate correlation between K-band magnitude and redshift. Our faintest (S/N=3σ) unresolved sources near $K_s \approx 19.5^m$ would include galaxies with redshifts in the range $0.4<z<1.5$ if they were present in the field.

Deep K-band galaxy counts by Gardner (1995) yield an expected surface density of galaxies with magnitudes between $+18^m$ to $+20^m$ of 10,000/deg^2, which implies that in Patch 3 we should see ~ 200 galaxies. The contribution by faint galaxies to the integral star counts for Patch 3 is shown in Figure 16. The figure shows that, at the galactic latitude of Patch 3, the contribution to the point source counts by distant, faint galaxies is significantly smaller than the expected number of foreground stars at the same latitude. Discrete source counts are, therefore, dominated by foreground stars for magnitudes brighter than $\approx +20.0^m$. Figure 17(b) also shows, for the sources identified by SExtract, that the discrete sources in Patch 3 fainter than $+17^m$ in K_s band are completely unresolved by 2MASS. We conclude that our clipping algorithm removes a significant number, and very likely all, of the resolvable galaxies to redshifts of $z \approx 1$, although our clipping procedure may still leave dwarf galaxies, or other local, low-surface brightness systems present in the data.

Based upon the previous discussions, we can summarize the likely contributions to the background fluctuations from non-cosmological foreground sources in Table 3. In columns 2 and 3 we indicate the estimated color of each component. In column 4 we give the mean background intensity over the full field-of-view, and in column 5 we estimate the background fluctuation expected at a scale of approximately one arcminute.

5. Conclusions

By using the calibration field data from 2MASS, we have created a deep-integration field at J, H and K_s bands covering an area of $8.5' \times 1^\circ$. After clipping out all foreground point sources brighter than the K_s magnitude of $\sim +19^m$ we detect a statistically significant structure of the residual diffuse emission. The angular power spectrum of this emission has a power law dependence with the slope expected from that of the CIB due to clustered galaxies. The cosmological part of this and its implications are discussed in the companion

paper KOMSC.

We demonstrated in this paper that the various foreground (atmospheric, zodiacal and Galactic) contributions to the residual diffuse background are small and in any case would be of different angular slope. The color of these components would likewise be very different from the color of the found signal. This is consistent with the signal being due to CIB from early galaxies.

We note in conclusion that the amplitude of the signal is broadly consistent with other findings on larger angular scales by KO from the COBE DIRBE and Matsumoto et al. (2000, 2002) from the IRTS mission. E.g. the KO analysis suggested a CIB fluctuation of $5.9^{+1.6}_{-3.7}$ nWm^{-2}sr^{-1} in the DIRBE K band at $\sim 0.5^{\circ}$ scale when all galaxies are included. That was also confirmed in the IRTS findings of Matsumoto et al. (2000, 2002). In this study we detect an amplitude in K_s band of ~ 10 nWm^{-2}sr^{-1} at $\sim 1.5'$ after removing all galaxies out to $K_s \simeq 18.5$ consistent with the above after accounting for the difference in angular scales and the contribution from the removed galaxies (KOMSC). Our results lend further support to the emerging body of evidence that the CIB levels are significantly higher than what can be produced by the observed populations of galaxies (KO, Wright & Reese 2000, Cambresy et al. 2001).

Acknowledgments

This publication makes use of data products from the Two Micron All Sky Survey, which is a joint project of the University of Massachusetts and the Infrared Processing and Analysis Center/California Institute of Technology, funded by the National Aeronautics and Space Administration and the National Science Foundation.

We would like to thank Dr. Rick Arendt for his careful reading of the manuscript and his assistance in using the DIRBE Faint Source Model and SExtract. We would also like to thank Ms. Destiny Coslett at Long Reach High School in Columbia, Maryland

for her assistance in the photometry of the faint sources in Patch 3. Her assistance in identifying and cataloging standard star field scans in the 2MASS scan archive was also greatly appreciated.

REFERENCES

Abraham, P. et al. 1998, in 'The Universe as seen by ISO', P. Cox and M.F. Kessler eds., ESA Publication Division, Noordwijk, pp 145-148.

Arendt, R. et al. 1998, Ap.J., **508**, 74.

Beckwith, S. et al. 1976, Ap.J., **208**, 390.

Bernstein, R.A., Freedman, W.L. and Madore, B. 2002, Ap.J (In Press)

Bertin, E., Arnouts, S. 1996, A& A, **117**,393.

Cambresy, L. et al. 2001, Ap.J. **555**, 563

Casali, M.M., and Hawarden, T.G. 1992, JCMT-UKIRT Newsletter No. 4, 33

Cowie, L., Songaila, A., Hu, E. and Cohen, J. 1996, AJ **112**, 839.

Cutri, et al. 2001. 2MASS Explanatory Supplement.

http://www.ipac.caltech.edu/2mass/releases/second/doc/explsup.html

Djorgovski, S. et al. 1995, ApJ (Letters) 438, L13.

Dwek, E. and Arendt, R. 1998, Ap.J. **508**, L9.

Dwek,E., et al. 1998, Ap.J., **508**,106.

Fall,S.M., Charlot, S. and Pei, Y 1996,Ap.J.Lett,**464**,L43.

Gardner, J.P., 1995, Ap.J. **452**, 538.

Gardner, J.P., et al. 1997, Ap.J.,**480**, L99.

Gautier, N. et al., 1992. AJ, **103**, 1313.

Gorjian, V. Wright, E. and Chary, R. 2000, Ap.J. **536**, 550.

Guhathakurta, P. & Cutri, R.M. 1994, in 'The First Symposium on the Infrared Cirrus and Diffuse Interstellar Clouds", ASP Conference Series, Vol. 58, 1994, R.M. Cutri and W.B.

Latter, Eds., p.34

Hauser, M. and Dwek, E. 2001. Ann. Rev. Astro. and Astrop. **39**, 249.

Huang, J.-S., et al., 1997, ApJ, 476, 12.

Kashlinsky, A., Mather, J., Odenwald, S. and Hauser, M. 1996,Ap.J.,**470**,681. (Paper I)

Kashlinsky, A., Mather, J., and Odenwald, S. 1996, Ap.J.Lett.,**473**,L9. (Paper II)

Kashlinsky, A. and Odenwald, S. 2000,Ap.J.,**528**, 74. (Paper III)

Kashlinsky, A., Odenwald, S., Mather, J., Skrutskie, M. and Cutri, R. 2002, Ap.J.(Letters), submitted. (KOMSC)

Kauffmann, G. and Charlot, S. 1998, MNRAS **297**, L23

Madau, P. et al. 1996, MNRAS, **283**, 1388.

Malkan, M. and Stecker, T. 2001, Ap.J, **555**, 641.

Matsumoto, T. et al. 2000, in 'ISO Survey of a Dusty Universe', D. Lemke, M.

Matsumoto, T. et al., 2002, Ap. J., (Submitted)

Nikolaev, S. et al. 2000, A.J. 120, 3340.

Stecker, F. W. & De Jager, O. C. 1993, Ap.J.,415,L71

Stickel, eds. (Berlin and Heidelberg: Springer-Verlag), 96.

Persson, S., et al., 1998 AJ, **116**, 2475.

Ramsay, S.K. et al., 1992. MNRAS **259**, 751.

Reach, W. 1992, Ap.J, **392**, 289.

Reach ,W. et al 1995, Nature **374**, 521.

Skyes, M., 1988, Ap.J(Letters) **334**, L55.

Vogeley, M. 1997, AAS. 191, 304. (astro-ph/9711209).

Wright, E. L., 1998, Ap.J, **496**, 1.

Wright, E. L. & Reese, E.D. 2000, Ap.J., 545, 43.

Table 1. Selected faint stars in the P565-C region

Star	m_J	m_H	m_{K_s}	[J-H]	[H-K_s]
4	20.0 (8.4)	19.2 (4.4)	18.9 (6.5)	+0.8	+0.3
11	19.4 (9.2)	18.5 (16.4)	18.3 (5.0)	+1.1	+0.2
16	20.7 (4.5)	20.5 (2.9)	19.4 (3.9)	+1.3	+1.1
17	20.0 (7.5)	19.3 (2.4)	19.2 (5.0)	+0.8	+0.1
22	19.7 (4.3)	19.7 (2.6)	19.4 (4.2)	+0.3	+0.3
28	20.2 (2.6)	19.5 (3.2)	18.6 (4.0)	+1.6	+0.9

Table 2. Clipped Patch Data

Name	$f(\%)$	$< N >$	$m_J(\sigma)$	$m_H(\sigma)$	$m_{K_s}(\sigma)$
1	94	475	+21.2 (56)	+20.5 (52)	+20.1 (36)
2	92	519	+20.4 (98)	+20.1 (75)	+19.7 (49)
3	93	482	+21.3 (48)	+20.5 (47)	+20.1 (32)
4	94	520	+20.1 (62)	+20.3 (65)	+19.8 (44)
5	93	489	+21.3 (46)	+20.5 (55)	+20.1 (33)
6	92	509	+20.9 (70)	+20.3 (62)	+20.1 (39)
7	94	472	+20.9 (67)	+20.2 (65)	+19.8 (45)

Table 3. Limits to Foreground Fluctuation Contributions

Component	[J-H]	[H-K]	$I_\nu(K_s)$ (MJy/sr)	K-band Fluctuation (nWm^{-2}sr^{-1})
Atmosphere + Instrument	+1.9	+1.2	295	<2
Zodiacal Light	+0.4	-0.3	0.1	< 1
Cirrus/DISM	-0.6	-1.1	0.2	1
Diffuse Star Light	+0.5	+0.7	0.2	< 9

Figure 1: Histogram of the background noise dispersion for all of the 2MASS images employed in this analysis for J-band (solid), H-band (dotted) and K_s band (dashed).

Figure 2: Histogram of the number of co-adds in each pixel for the final image in K_s band.

Figure 3: (Top) Individual 2MASS images for 7.8-second integration in J, H and K_s band. (Bottom) Corresponding deep-integration co-added images for an effective integration time of 3,900 seconds.

Figure 4: Co-added calibration strip divided into seven patches as described in the text. Actual sky image is shown in the left-hand columns. Distribution of pixel samples employed to construct the averages in the integrated images shown in the right-hand columns.

Figure 5: (a) Left: Color-color plot of the various emission components in Patch 3. The plotting symbols indicate the following features: (X symbols) indicate the color corresponding to the arc-second scale power spectrum amplitude for all seven image patches. (Ring) circumscribes the data for 10^5 unresolved objects in the 2MASS Point Source Catalog. (Diamond) The mean color of the stars photometered in Patch 3. (Triangle) is the predicted zodiacal light emission. (Square) indicates the mean color of the atmosphere obtained from an average of the 2080 images with 1-σ error bars. (Asterisk) is the residual emission of the background of the co-added, clipped Patch 3 field. (b) Right: Color-magnitude plot of faint point sources in Patch 3.

Figure 6: Power spectrum of a single, 7.8-second image showing (lower curve) the influence of the beam and (top curve) the beam-subtracted spectrum.

Figure 7: Power spectrum of the K_s band Patch 3 region showing: (top curve) the power-law residual and (bottom points) the white-noise contribution from atmospheric+instrument noise.

Figure 8: Power spectrum of deep-integration field in J, H and K_s bands showing the vertical and horizontal 'artifact' caused by striping effects in the original image.

Figure 9: Comparison of the seven patch sigmas in J (triangles), H (squares) and K_s (crosses) bands before (horizontal axis) and after (vertical axis) Fourier filtering to remove the striping artifacts.

Figure 10: Power spectra of each of seven patches in each band. The value for the background sigma employed in clipping point sources is indicated in each panel.

Figure 11: Variation of the background noise dispersion for each image as a function of airmass. The dispersion is given in units of $\mathrm{nWm^{-2}sr^{-1}}$.

Figure 12: Distribution of the background pixel intensities following clipping for J, H and K_s bands in Patch 3.

Figure 13: Image of clipped field for Patch 3 in K_s band to show the locations of clipped pixels and the smoothness of the remaining background emission. The gray scaling range extends from -5 to +5 $\mathrm{nWm^{-2}sr^{-1}}$.

Figure 14: Power spectrum of the A-B Patch 3 field in J, H and K_s bands.

Figure 15: Shows the power spectrum for the unclipped Patch 5 (diamonds) and its residual power spectrum after clipping and destriping (plus signs). This is juxtaposed against a test field with 7.8 sec exposure in the Galactic plane located at Galactic $(l, b) = (358.9°, -21.6°)$ which contains a comparable number of stars to that in Patch 5 at the final co-add. The fraction of the pixels clipped in the former is about 14%. The power spectrum for unlicpped test field is shown with open triangles; it is scaled to the unclipped power spectrum for Patch 5. The power spectrum for the clipped test field is shown with dots with the error bars.

Figure 16: Cumulative point source counts, N(m), in Patch 3 (triangles). The vertical

axis is in units of Log(stars/deg^2). Error bars reflect the statistical uncertainty in the number of counted stars in Patch 3 in each magnitude bin. Also shown (solid line) is the predicted number of stars based on the DIRBE Faint Source Model, and the expected number of galaxies (dashed line) according to a summary by Djorgovski et al. (1995).

Figure 17: (a) Left: Histogram of the rms radii of the discrete sources identified by SExtract in Patch 3 in K_s band. (b) Right: Variation of the angular sizes of the discrete sources identified by SExtract, versus their integrated K_s magnitude.

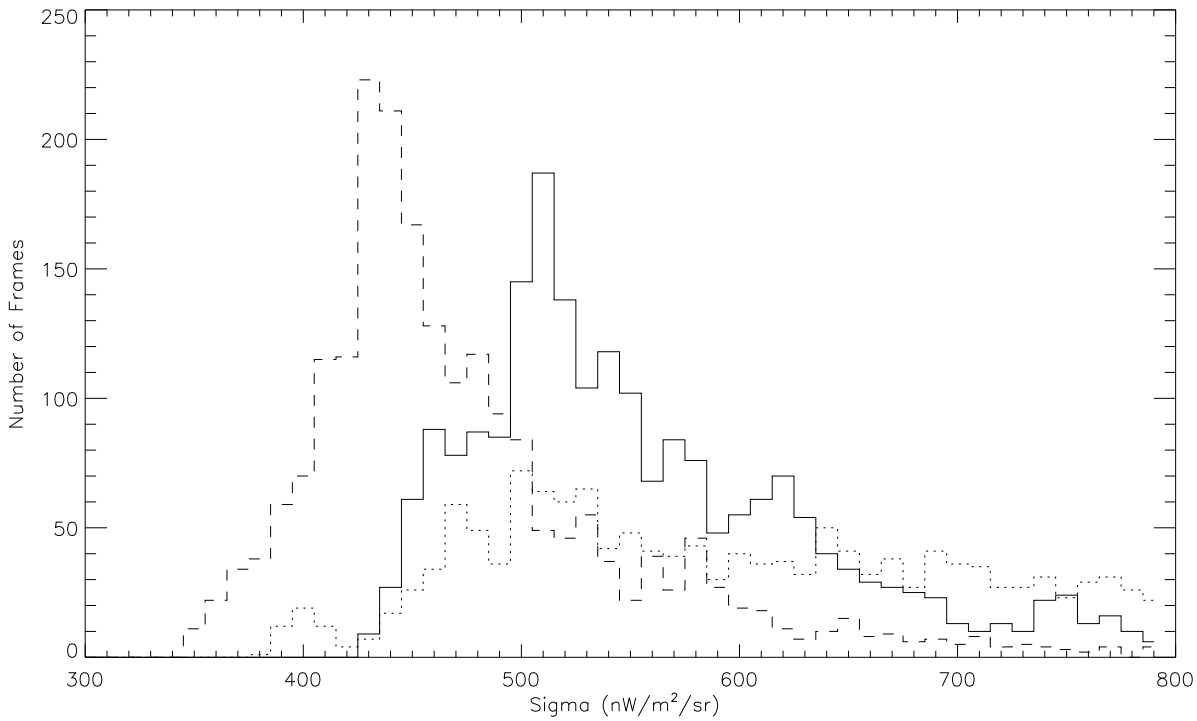

Fig. 1.— Figure 1

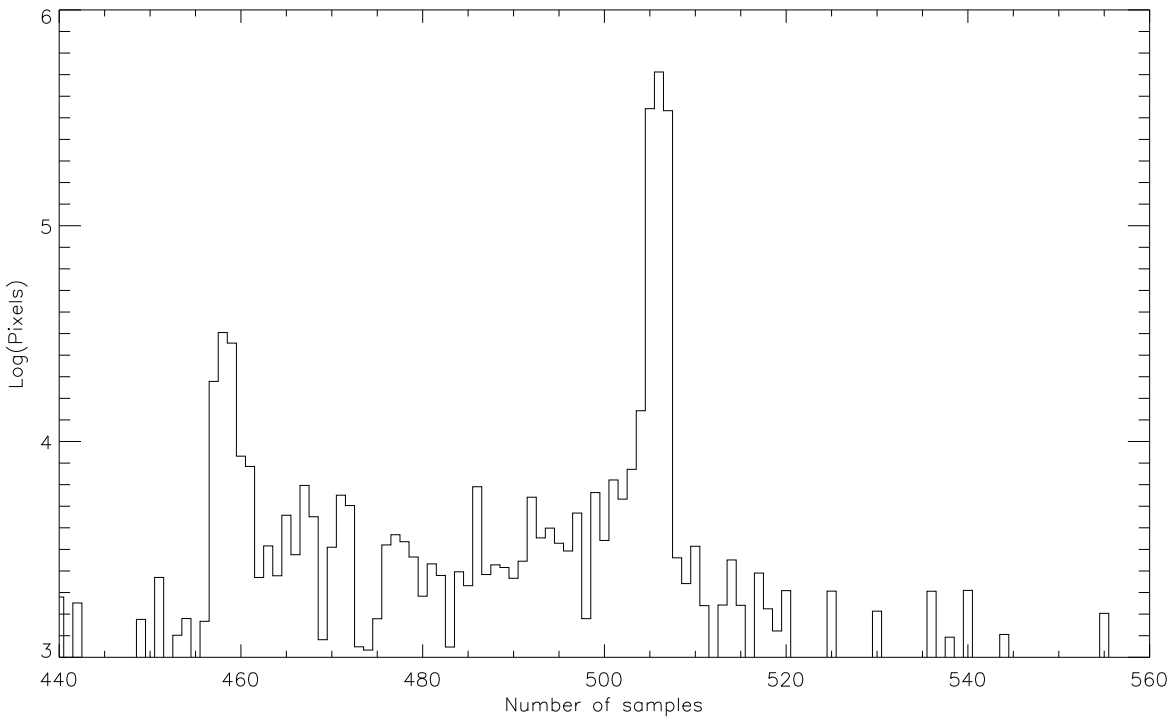

Fig. 2.— Figure 2

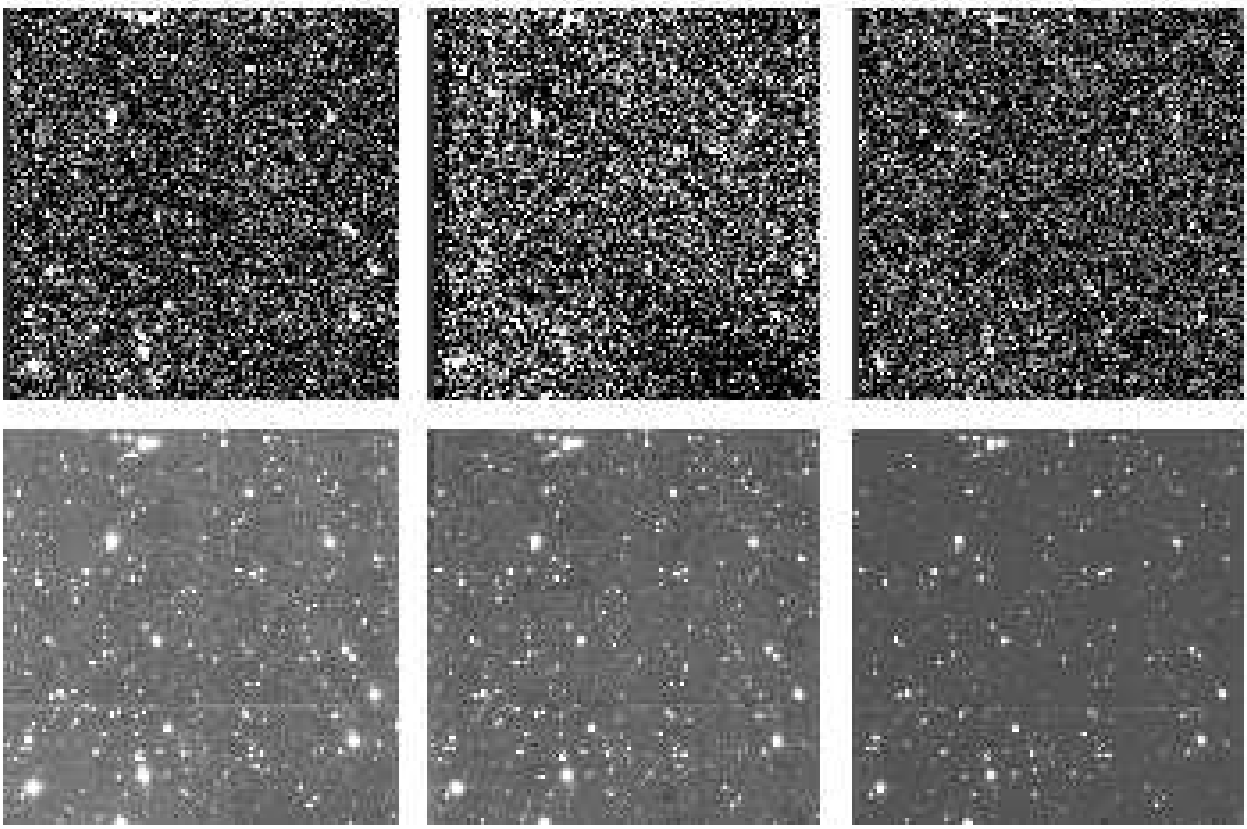

Fig. 3.— Figure 3

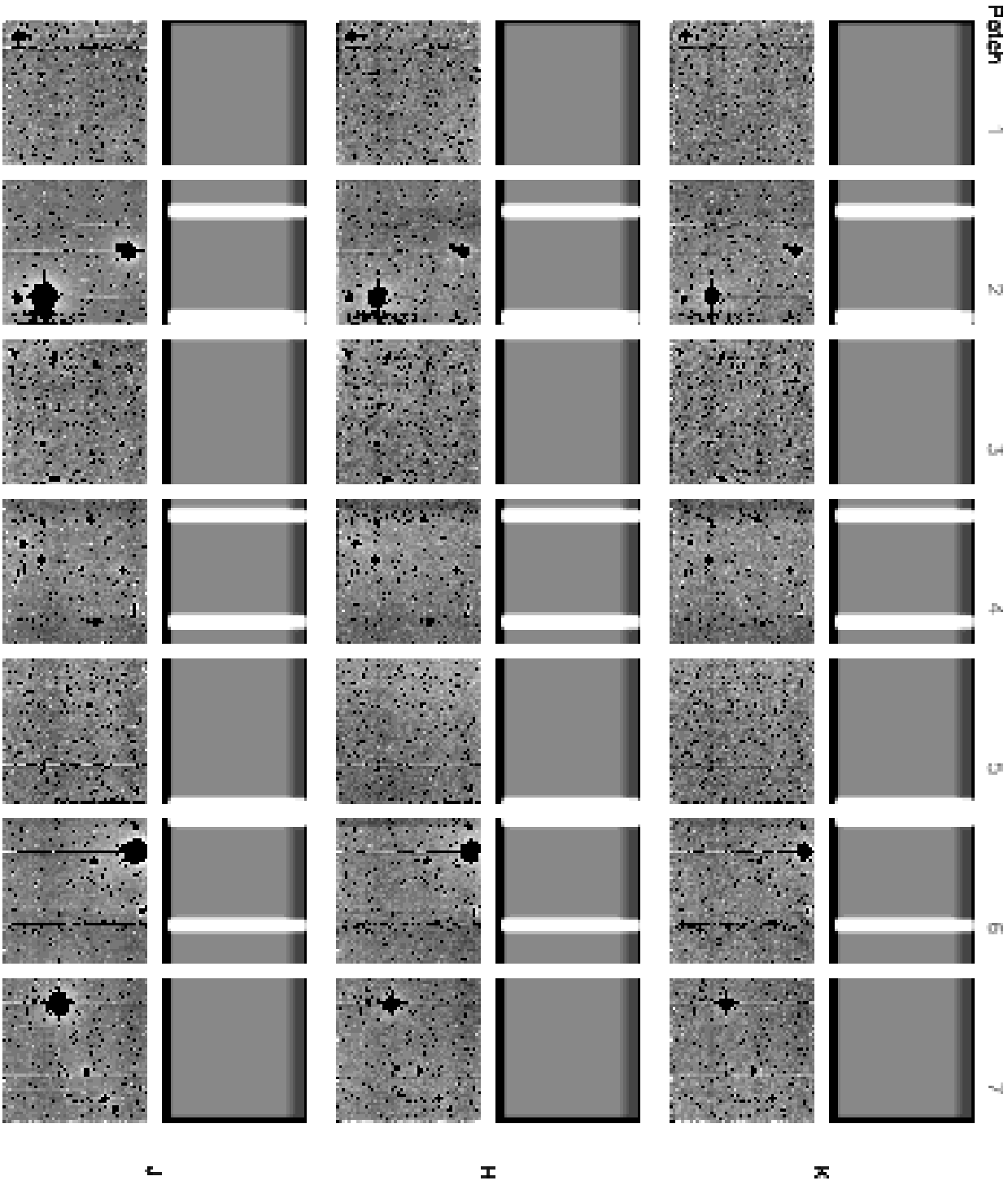

Fig. 4.— Figure 4

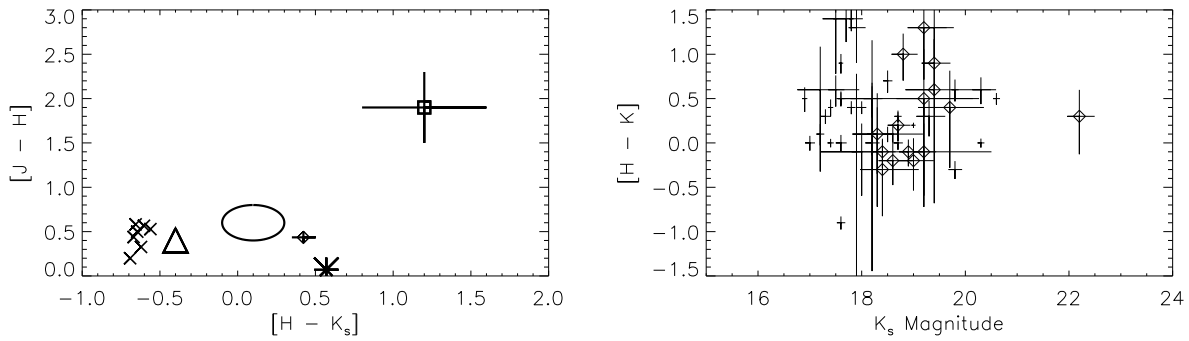

Fig. 5.— Figure 5

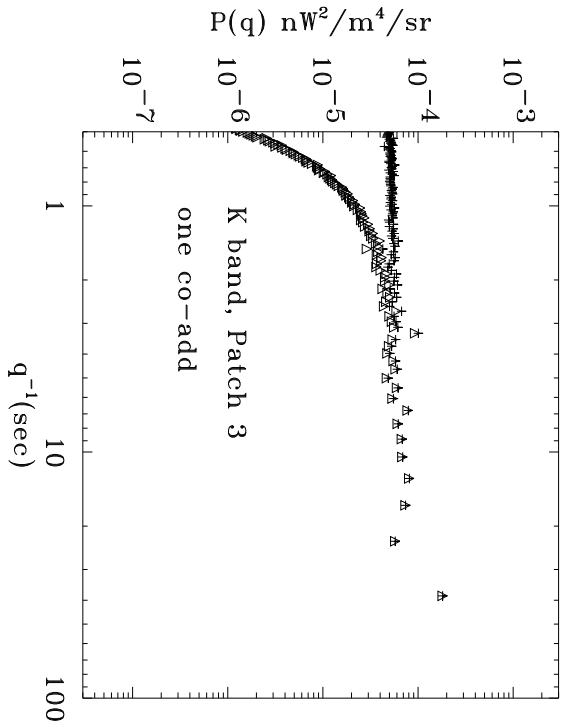

Fig. 6.— Figure 6

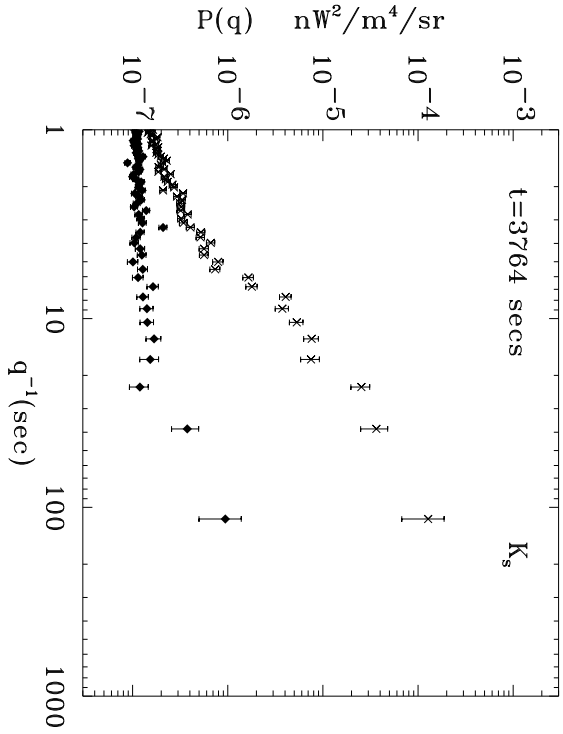

Fig. 7.— Figure 7

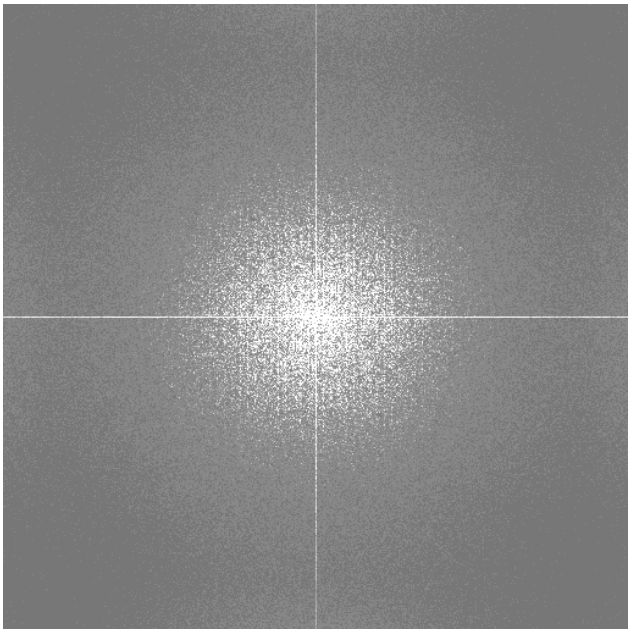

Fig. 8.— Figure 8

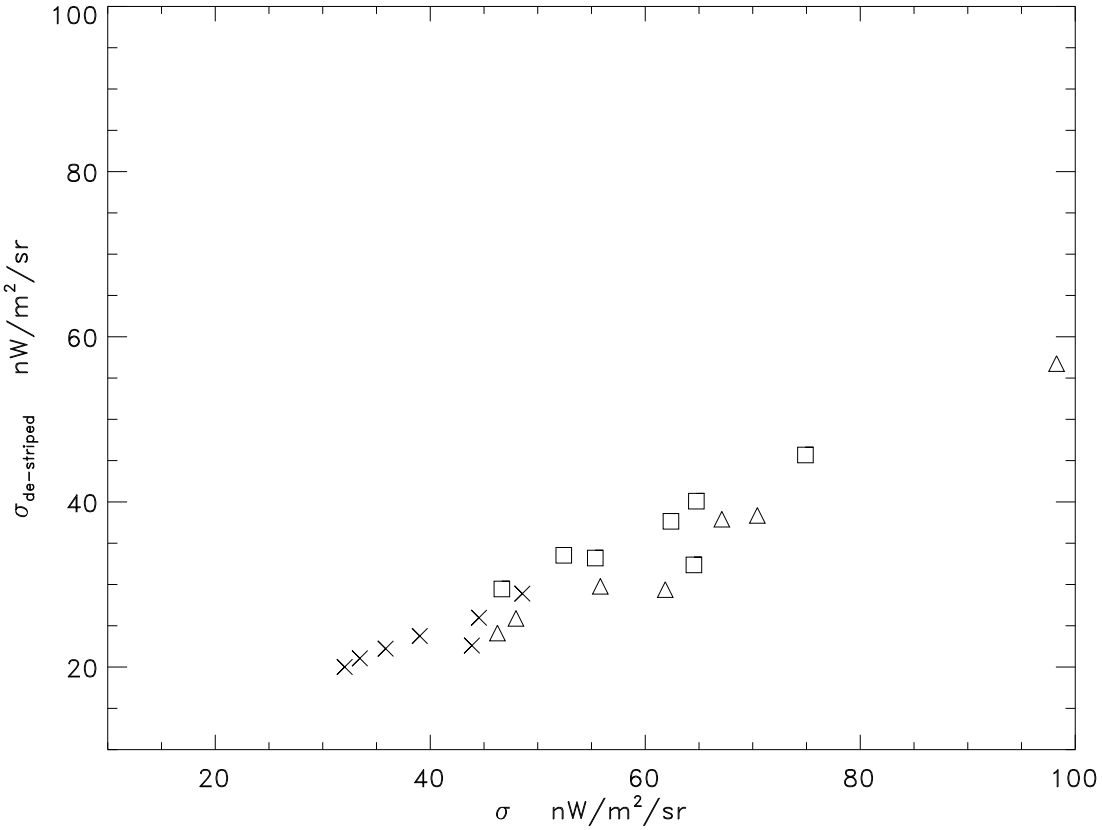

Fig. 9.— Figure 9

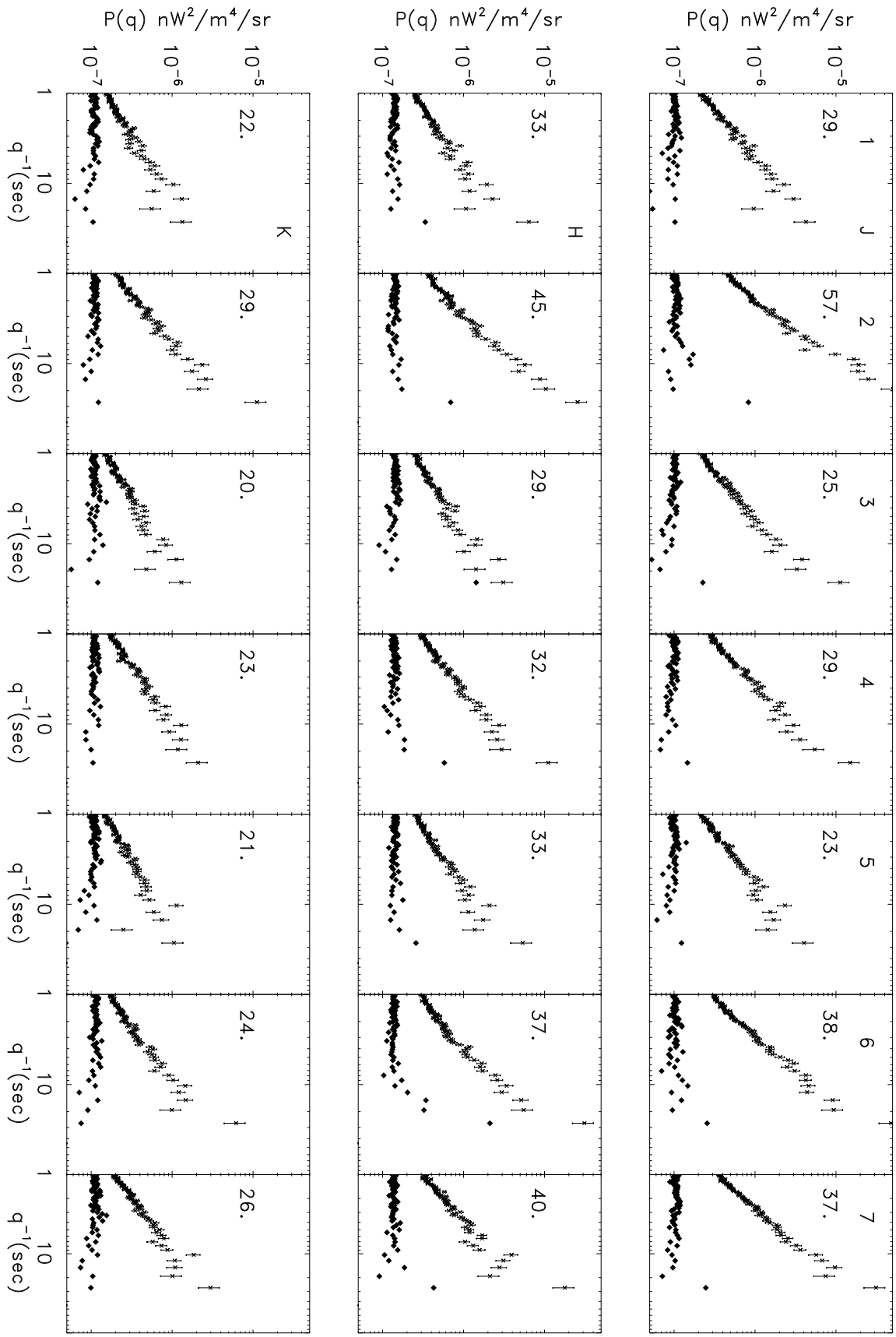

Fig. 10.— Figure 10

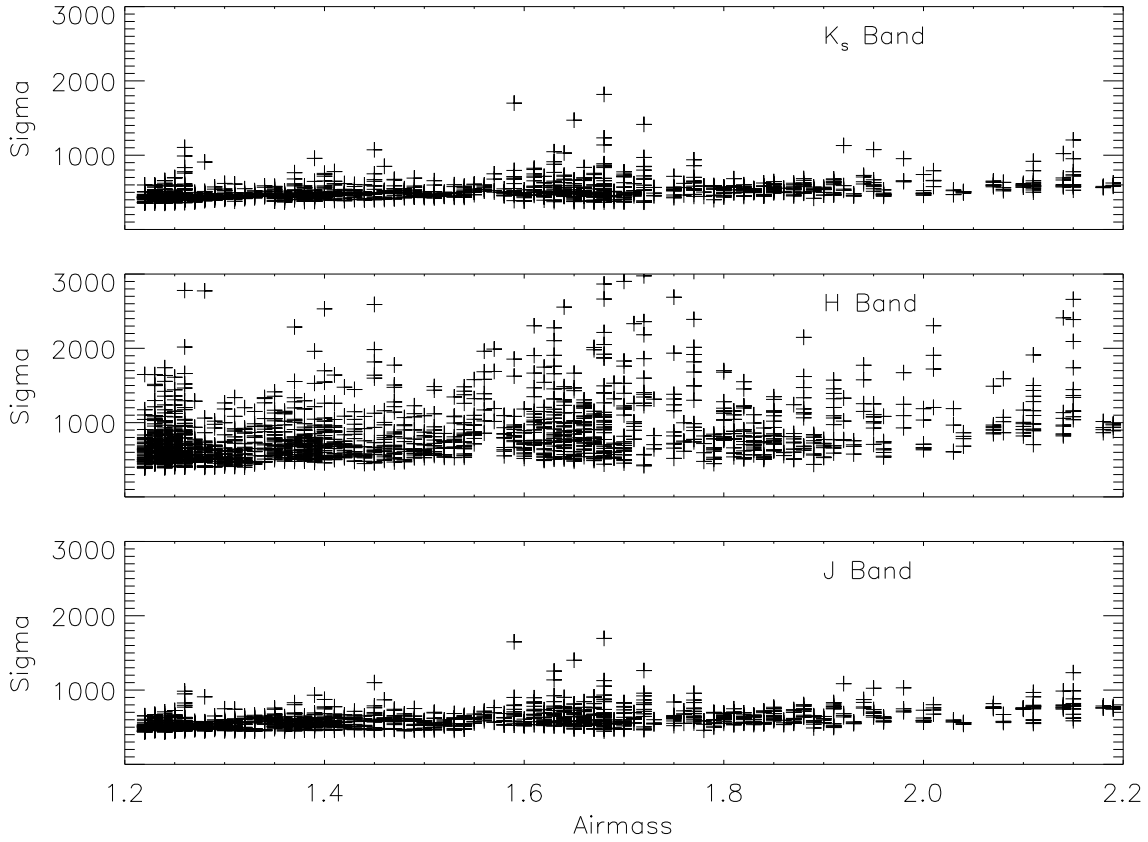

Fig. 11.— Figure 11

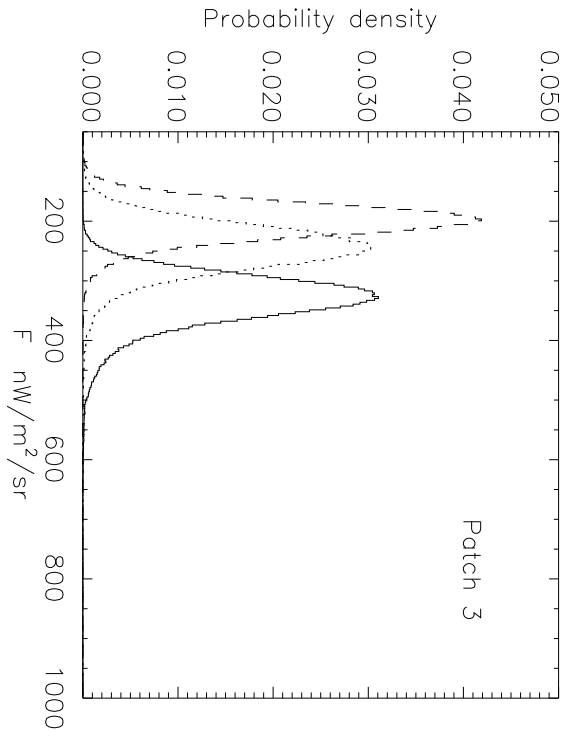

Fig. 12.— Figure 12

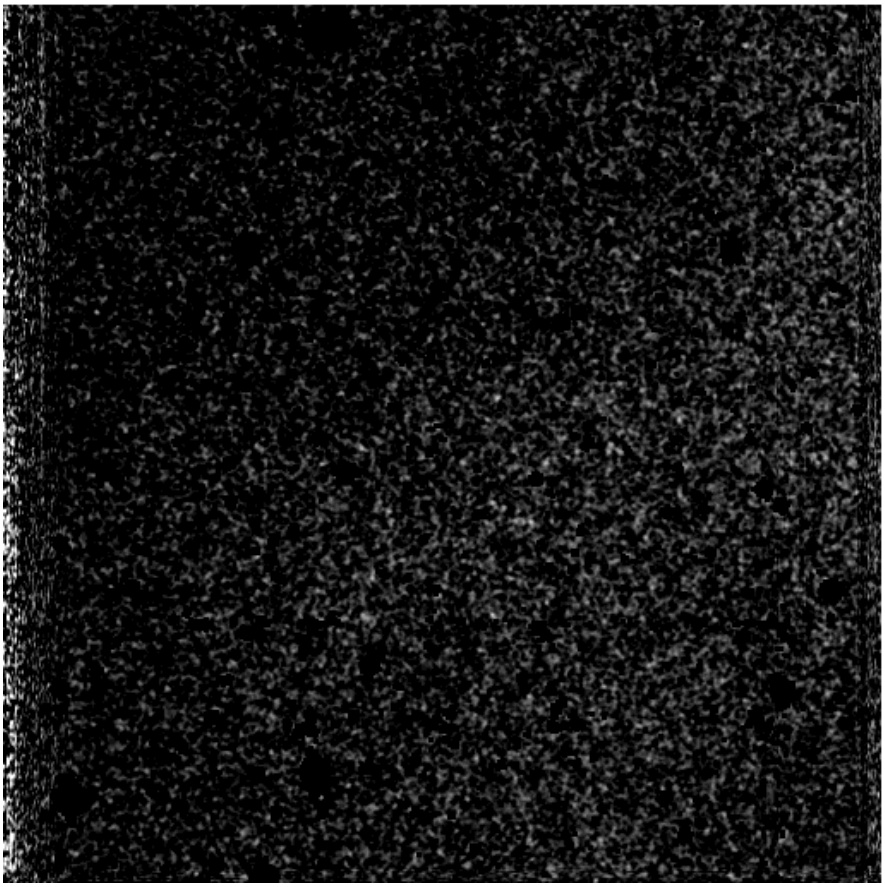

Fig. 13.— Figure 13

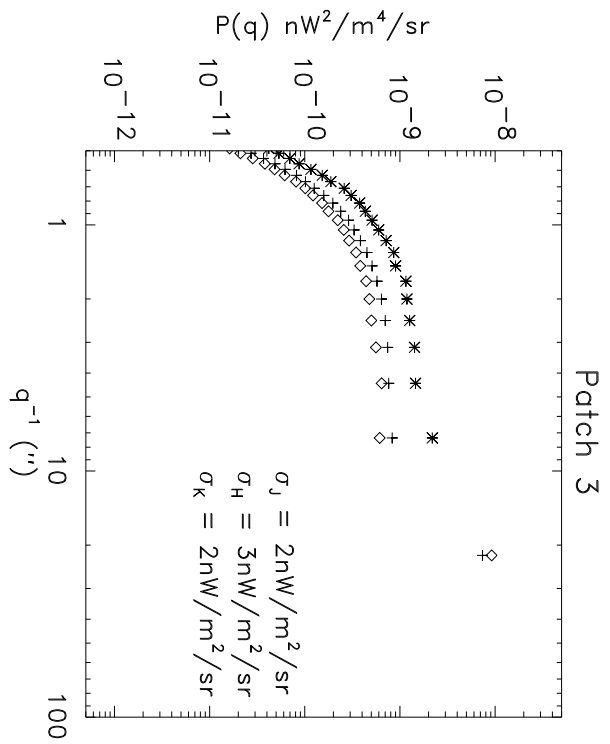

Fig. 14.— Figure 14

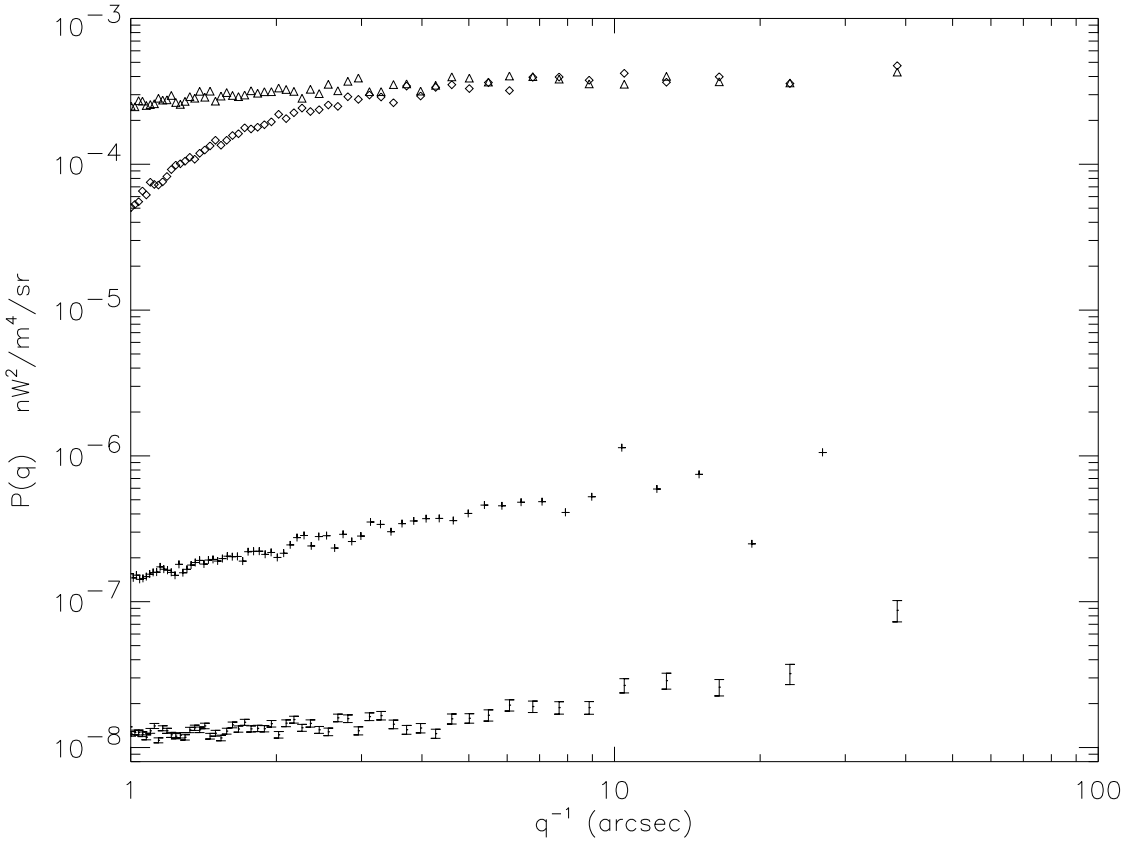

Fig. 15.— Figure 15

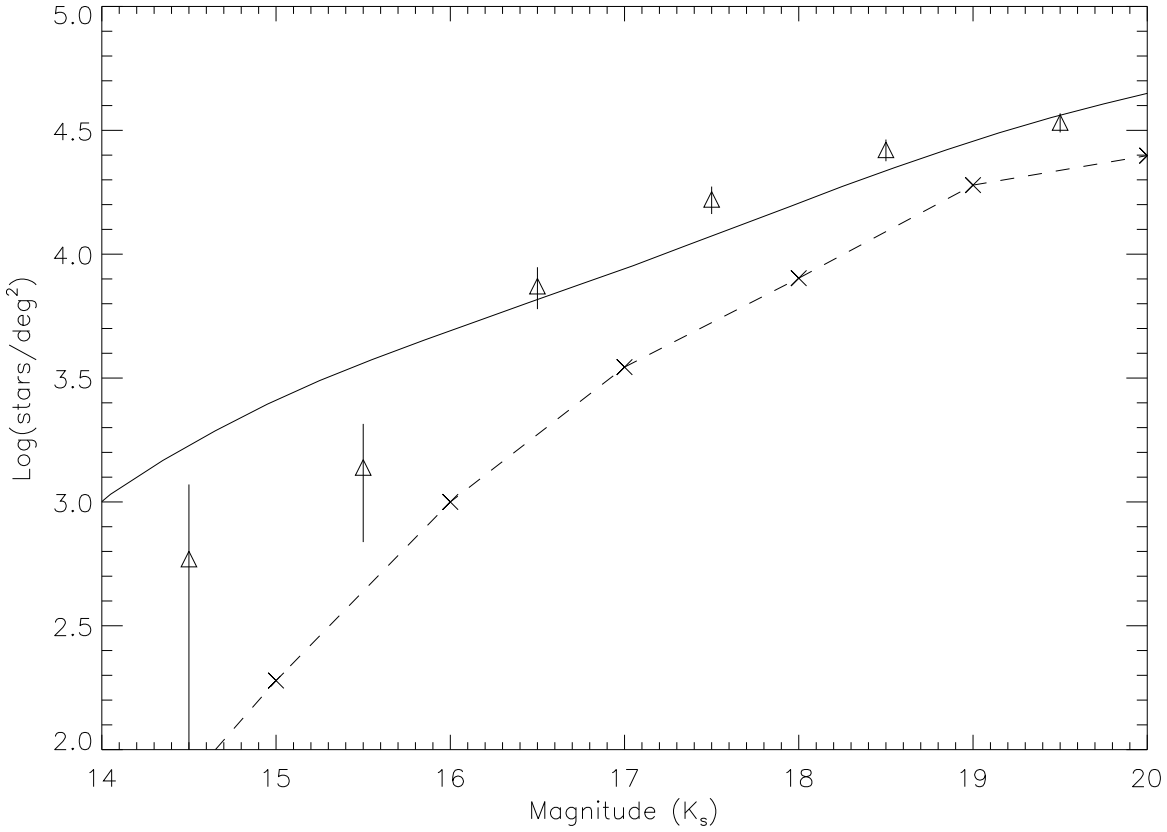

Fig. 16.— Figure 16

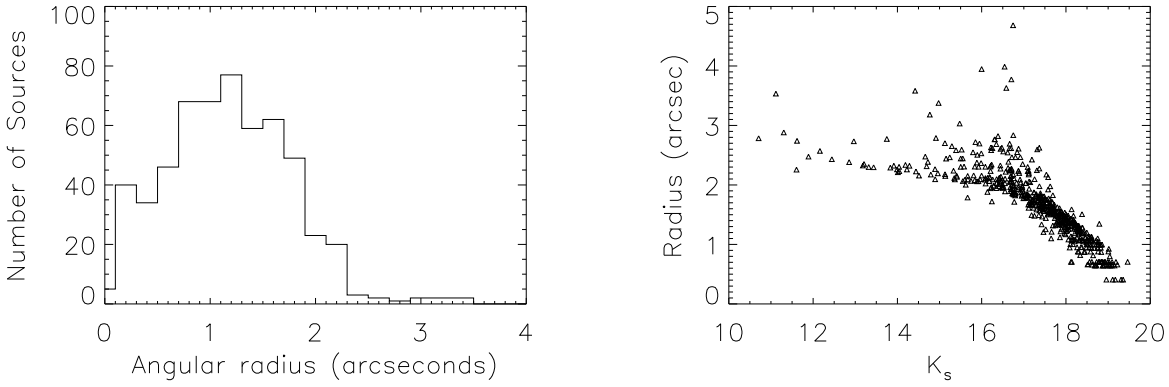

Fig. 17.— Figure 17